Journal of Alloys and Compounds 507 (2010) 126–132

Contents lists available at ScienceDirect

Journal of Alloys and Compounds

journal homepage: www.elsevier.com/locate/jallcom

Temperature dependent dielectric characterization of manganese dioxide nanostructures with different morphologies at low frequency

Hongtao Guan*, Gang Chen, Jing Zhu, Yude Wang

Department of Materials Science and Engineering, Yunnan University, 650091 Kunming, People's Republic of China

ARTICLE INFO

Article history:
Received 8 July 2010
Accepted 18 July 2010
Available online 23 July 2010

Keywords:
Manganese dioxide
Microrods
Nanowires
Dielectric properties

ABSTRACT

The β-MnO_2 microrods and α-MnO_2 nanowires were prepared with hydrothermal methods at 160 °C for 48 h. The effects of the reactant concentrations on the crystal structures and morphologies of the samples were carried out. Analytical methods such as X-ray diffraction (XRD), scanning electron microscopy (FESEM), and transmission electron microscopy (TEM) were employed to characterize the morphology and microstructure of the final products. The temperature dependent of dielectric properties of the samples from 223 K to 393 K were also characterized and discussed in detail. The results show that the crystal structures and morphologies of the samples change with the $KMnO_4$ concentration from β-MnO_2 pyramidal microrods with diameters 2–3 μm and lengths 3–6 μm to α-MnO_2 nanowires with 30-nm-diameters and 1-μm-lengths. The dielectric constants and the dielectric loss tangents decrease with the frequency but increase with the temperature. The samples prepared at moderate $KMnO_4$ concentration, which contains both nanowires and microrods in the systems, show the best dielectric permittivity and loss tangents.

1. Introduction

With the development of low dimensional nano-sized materials and nanostructures, dimensionality and size of the materials have been regarded as critical factors that may bring some novel and unexpected characteristics in electronics, photonics, and catalysis [1]. In this sense, the shape- and size-controlled dispersible inorganic nanocrystals have become the candidates for investigations about their optical, electrical, magnetic and electromagnetic characteristics. Especially, their dielectric and electromagnetic wave (EMW) absorbing properties have aroused great interest because of the more and more civil, commercial and military applications in electromagnetic interference (EMI) shielding and absorbing materials [2].

Manganese dioxide is one of the most attractive inorganic materials because of its wide range of applications in catalysts, molecular-sieves, and ion-sieves due to its ion-exchange, molecular adsorption, catalytic, electrochemical, and magnetic properties [3,4]. The basic unit of manganese dioxide is the octahedral [MnO_6] close-packed structure, which is built up by one manganese atom coordinated with six oxygen atoms. These [MnO_6] units are linked together in different ways so as to form various crystallographic and derivative structures [5]. Since the first use of MnO_2 as an additive to battery by Leclanché, is has become the most widely used electrode materials [6]. Also, MnO_2 is one of the most important materials of manganese ferrites, and the influence of MnO_2 addition on the electromagnetic properties of ferrite material has caught most researchers' attention and significant progress has been made during the past few years [7]. However, most of the recent publications about MnO_2 materials are mainly focused on the formation mechanism and morphological characterizations of MnO_2 nanoparticles and some magnetic or electromagnetic studies [8–15]. Duan et al. studied the microwave absorbing properties of flake-like α-MnO_2/carbon black double-layer plate composites and revealed this composite had an −10 dB absorbing frequency band as wide as 8.6 GHz [9]. Yan et al. studied the electromagnetic properties of 3D sponge-like porous γ-Mn_2O_3 materials and the results showed that the Mn_2O_3/paraffin wax had one absorption peak value of about −17.6 dB at 16.6 GHz with a thickness of 6 mm [10]. Our early studies on the dielectric and microwave characteristics of pyrolusite MnO_2 particles with flake- and strip-shaped structures also found that the MnO_2/SiO_2 composites with PVA as the binder had an absorbing peak value of about −25 dB at 8.5 GHz with a 30 vol% introduction [11,12]. As to the magnetic properties of MnO_2 materials, Liu and Yue have investigated the hysteresis loop characteristics of β-MnO_2 and α-MnO_2 nanorods at room temperatures, respectively and found that they all exhibited ferromagnetic properties with high coercivity values [13,14]. Wang et al. studied the magnetic properties of β-MnO_2 nanowires with a superconducting quantum interference device (SQUID) magnetometer and

* Corresponding author.
E-mail address: htguan06@ynu.edu.cn (H. Guan).

0925-8388/$ – see front matter © 2010 Elsevier B.V. All rights reserved.
doi:10.1016/j.jallcom.2010.07.135

evidenced a higher Néel magnetic transition temperature than bulk MnO_2 crystal and the existence of a superparamagnetic state at 293 K [15].

The intrinsic structure and morphology of the MnO_2 particulates have great effects on their final properties and so the electromagnetic properties of the ferrite materials. MnO_2 materials with different crystallographic forms have different tunnel structures, and the temperature will affect the dispersion of other charge carriers such as atoms and molecules in the interior tunnels and cavities, which leads to the fact that MnO_2 materials will have various dielectric relaxation phenomenon and electromagnetic characteristics with temperature. Shi et al. [16] have studied the high temperature dielectric properties of β-MnO_2 nanorods at the temperature range of 293–773 K and found an increase of dielectric loss tangents with temperature due to the relaxation of the dipole molecules in cooperation with the drop in the relaxation time. To our knowledge, however, there are no public reports on the temperature dependence of electromagnetic properties of MnO_2 materials at low temperature and low frequency ranges.

In this study, β-MnO_2 microrods and α-MnO_2 nanowires have been hydrothermally synthesized at 160 °C for 48 h through controlling the reactant concentrations. The exterior morphologies and structures were characterized by scanning electron microscopy (SEM), high-resolution transmission electron microscopy (HRTEM) and X-ray diffraction (XRD). The influence of reaction concentrations on the final products and their characteristics was discussed detailedly. Their complex permittivity variations with temperature and frequency were also measured and discussed at the frequency between 1 kHz and 1 MHz.

2. Experimental

2.1. Preparation of nanostructured manganese dioxides

All the chemicals were of analytical grade and used as received without any further purification. Deionized water was used throughout the experiments. The chemical reaction for the synthesis of MnO_2 nanostructures can be expressed as below:

$$3MnSO_4{\cdot}H_2O + 2MnO_4^- \rightarrow 3SO_4^{2-} + 5MnO_2(s) + H_2O \quad (1)$$

In a typical procedure, 2 mmol $KMnO_4$ and 3 mmol $MnSO_4{\cdot}H_2O$ were dissolved in 80 ml deionized water successively at room temperature. After magnetically stirred for 30 min, the homogeneous dark brown solution was transferred into a Teflon-lined stainless steel autoclave. The autoclave was sealed and maintained at 160 °C for 48 h. After the reaction was completed, the autoclave was allowed to cool down to room temperature naturally. The resulting solid products were centrifuged and rinsed several times with deionized water and absolute ethanol, then finally dried at 100 °C for 8 h. The final black powder was collected for characterization. To examine the effect of concentration variations on the resulting products, the different $KMnO_4$ concentrations (0.025 M, 0.0625 M and 0.125 M) were used whilst maintaining the molar ratio of $KMnO_4$ to $MnSO_4{\cdot}H_2O$ as 2:3.

2.2. Characterization of nanostructured manganese dioxides

The phase identification was performed by X-ray diffraction (XRD, DSC-2000 X-ray diffractometer; CuKα radiation, λ = 1.54184 Å) in the range of $2\theta = 10°–90°$ in steps of 0.02°. The particle morphologies and selected area electron diffraction (SAED) were observed employing scanning electron microscopy (FESEM, HITACHI S-4800) and high-resolution transmission electron microscopy (HRTEM, Tecnai $G^2$20 S-Twin). The temperature dependences of the complex permittivity and dielectric loss tangents were examined by an impedance analyzer (Agilent 4294A) and Test Chambers (ESPEC SU-261). The as-prepared MnO_2 powders were mixed uniformly with polyvinyl alcohol (PVA) with a filling ratio of 85 wt.% and molded into plate specimens with diameters of 15 mm and thicknesses 1–2 mm. After heated at 60 °C for 24 h, the specimens were collected for microwave tests. The testing frequency ranges from 1 kHz to 1 MHz and the temperature is from 223 K to 393 K.

3. Results and discussion

Fig. 1 shows the XRD patterns of the samples synthesized at 160 °C for 48 h and subsequently dried at 100 °C for 8 h. It is clearly noted that the as-prepared products show different crystallinity

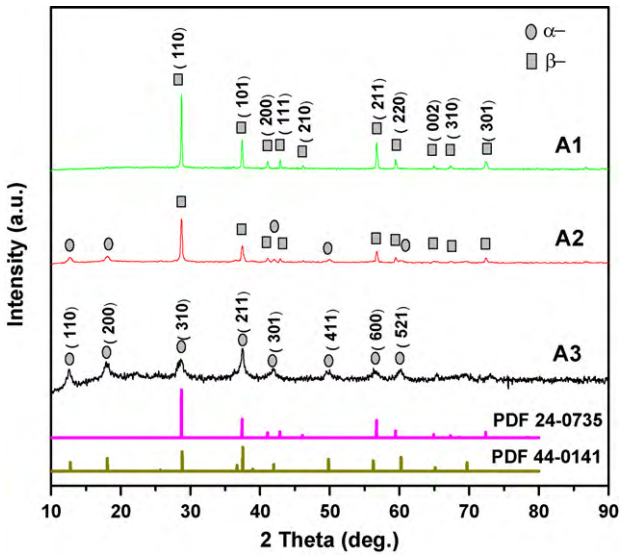

Fig. 1. The XRD pattern of MnO_2 hydrothermally synthesized at 160 °C for 48 h with different $KMnO_4$ concentrations: A1: 0.025 M, A2: 0.0625 M, A3: 0.125 M.

with the different $KMnO_4$ concentrations. The sample synthesized with $KMnO_4$ 0.025 M (sample A1) can be easily indexed to pure tetragonal β-MnO_2 phases (JCPDS 24-0735) with the space group *P*42/*mnm* (136). The well-developed reflections show the high crystallinity of the samples. With the $KMnO_4$ concentration increasing to 0.0625 M (sample A2), the diffraction peaks of α-MnO_2 (JCPDS 44-0141) begin to rise at 12.78° and 18.06°, corresponding to its (1 1 0) and (2 0 0) plane diffraction peaks. When the $KMnO_4$ concentration further increases to 0.125 M, however, the material shows well-developed diffraction lines of pure tetragonal α-MnO_2 phases (JCPDS 44-0141) with a space group *I*4/*m* (87), as is shown in Fig. 1. The results indicate that the polymorphic forms and crystallinity of MnO_2 products can be easily controlled by the reactant $KMnO_4$ concentrations. With the increase of $KMnO_4$ concentration from 0.025 M to 0.125 M, the products turn from β-MnO_2 phase to α-MnO_2 phase.

For the preparation of MnO_2 materials, the inorganic cations have profound effects not only on the purity, crystallinity and thermal stability of the final products, but also on its resulting tunnel structures [17]. The concentrations of K^+ ions are one of the key factors to controlled synthesis of MnO_2 with different phases and structures [1]. With the increase of $KMnO_4$ concentrations, the structures of the resulting product develop from 1×1 tunnels to 2×2 tunnels, which lead to the formation of α-MnO_2 phases.

The microstructures of the products with different $KMnO_4$ concentrations were examined by SEM and the results were shown in Fig. 2. For the sample A1 prepared with a $KMnO_4$ concentration of 0.025 M, the macroscopic microrods with the diameters of 2–3 μm and lengths 3–6 μm are observed, as is shown in Fig. 2(a). Along with several slim ones, the diameters and lengthens are about 50 nm and 1 μm, respectively. And it also can be seen from the insert in Fig. 2(a) that the microrods are not in the cylindrical shape, but in the shape of pyramids, which is in accordance with that reported in the literature [18]. It is clear that the microrods are single-crystal β-MnO_2 from Fig. 3(a) and (b), corresponding to its (1 1 0) plane with a spacing of about 0.314 nm. Both the HRTEM in Fig. 3(b) and the SAED pattern inserted in Fig. 3(a) indicate that the β-MnO_2 microrods are of high crystallization degree, which also agrees with the XRD patterns in Fig. 1.

When the concentration increases to 0.0625 M (sample A2), the products consist of both microrods and nanowires with α-MnO_2 and β-MnO_2 phases, and some nanowires are gradually absorbed

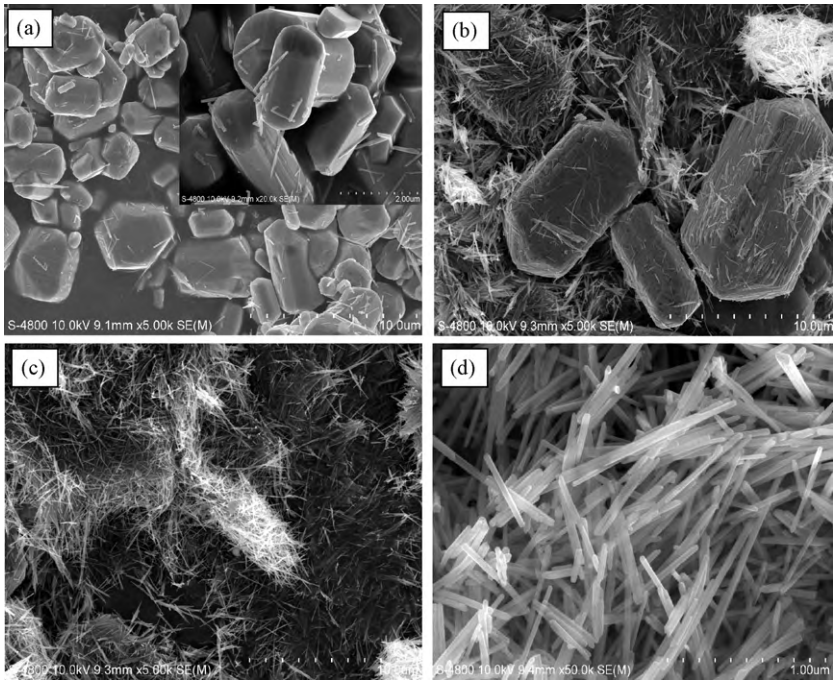

Fig. 2. SEM images of the MnO_2 samples prepared with different $KMnO_4$ concentrations: (a) sample A1, (b) sample A2, (c) sample A3, (d) high magnification image of A3.

by or self-assembled into bundles to form microrods as is shown in Fig. 2(b). The nanowires are in the diameters of nanometers and lengths several micrometers, and the microrods are about of 3–5 μm diameters and 10 μm lengths, which can also be observed from Fig. 2(b).

With the further increase of the $KMnO_4$ concentration to 0.125 M (sample A3), however, the products show pure α-MnO_2 nanorods. From Figs. 2(d) and 3(e), it is obvious that the nanorods are with diameters of 30 nm and lengths up to 0.5–1 μm. The interspacing distance of a single rod is about 0.702 nm, which corresponds to the (1 1 0) plane of α-MnO_2 phases.

From Fig. 3(f), it reveals crystal defects on the surface of the α-MnO_2 nanorods, which causes high surface energy, and makes the nanorods self-assembled to form bulk agglomerates, as is shown in Fig. 2(c). From Fig. 3(a), (c) and (e), it also illustrates that higher K^+ concentration is beneficial for the anisotropic growth of MnO_2 nanorods, and thus results in the transformation from β-MnO_2 microrods to much slim nanowires and nanorods of α-MnO_2 phases [1].

Generally, for a microwave absorbing material (MAM), the electromagnetic parameters, viz. complex permittivity ($\varepsilon_r = \varepsilon' - j\varepsilon''$), complex permeability ($\mu = \mu' - j\mu''$) and their loss tangent ($\tan\delta_e = \varepsilon''/\varepsilon'$, $\tan\delta_m = \mu''/\mu'$), are the quantified responses of molecules to an external electromagnetic field. The complex permittivity, along with the complex permeability, is introduced to allow for the electromagnetic losses due to the friction accompanying polarization and orientation of electric dipoles [19]. They all represent and determine the dielectric and magnetic properties of an absorbing material.

For a dielectric material, its permittivity can be represented by the Debye dipolar relaxation expression [20]:

$$\varepsilon_r = \varepsilon'(f) - j\varepsilon''(f) = \varepsilon_\infty + \frac{\varepsilon_s - \varepsilon_\infty}{1 + j\omega\tau_0} \quad (2)$$

where ω, τ_0, ε_s and ε_∞ are the angular frequency, macroscopic relaxation time, static dielectric constant and optical dielectric constant, respectively. From Eq. (2), the real and imaginary parts of the complex dielectric permittivity can be deduced as:

$$\varepsilon' = \varepsilon_\infty + \frac{\varepsilon_s + \varepsilon_\infty}{1 + \omega^2\tau_0^2}, \quad \varepsilon'' = \frac{(\varepsilon_s + \varepsilon_\infty)\omega\tau_0}{1 + \omega^2\tau_0^2} \quad (3)$$

From the above equations, one can see that dielectric permittivity is a complex function of both the frequency and temperature, apart from the dependence of other parameters such as pressure, etc. The temperature dependence of permittivity is mainly through the temperature dependence of the relaxation time τ, which can be expressed as [19]:

$$\tau = \tau_0 \exp\left(\frac{E_a}{kT}\right) \quad (4)$$

where τ_0 is the pre-exponential factor, k is the Boltzmann constant, T is the absolute temperature and E_a is the activation energy.

Fig. 4 shows the temperature dependent dielectric permittivity of samples A1, A2 and A3 at the different frequencies of 1 kHz, 10 kHz, 100 kHz and 1000 kHz and the temperatures ranging from 223 K to 393 K. Taking an overview of Fig. 4, it is clear that all samples exhibit the general trend of an increase in ε' with increasing temperature and a decrease of ε' with increasing frequency. Sample A3 prepared with the largest reactant concentration has the maximum values of dielectric constants at the same temperature, and A1 has the least values of permittivity in the whole temperature range at all frequencies. Take the frequency at 1 kHz for example, when the temperature changes from 223 K to 393 K, the permittivity of sample A3 increases from 35.3 to 133.6, however, the permittivity of sample A1 only changed from 13.3 to 36.1. At the same temperature of 293 K, when the frequency changes from 1 kHz to 1000 kHz, the permittivity of samples A3 turns from 60.2 to 7.1, and sample A1 changes from 23.2 to only 3.1.

As has known, α-MnO_2 and β-MnO_2 materials have aberrant octahedron structures with tunnels and cavities [21]. The tunnels and cavities make an entrance for other charge carriers such as atoms and molecules to enter the interior of manganese dioxide structures, which results in a local displacement and localized accumulation of charge carriers in the direction of electric field, so as to cause space charge polarization and interface polarization, which are the main causes for the dielec-

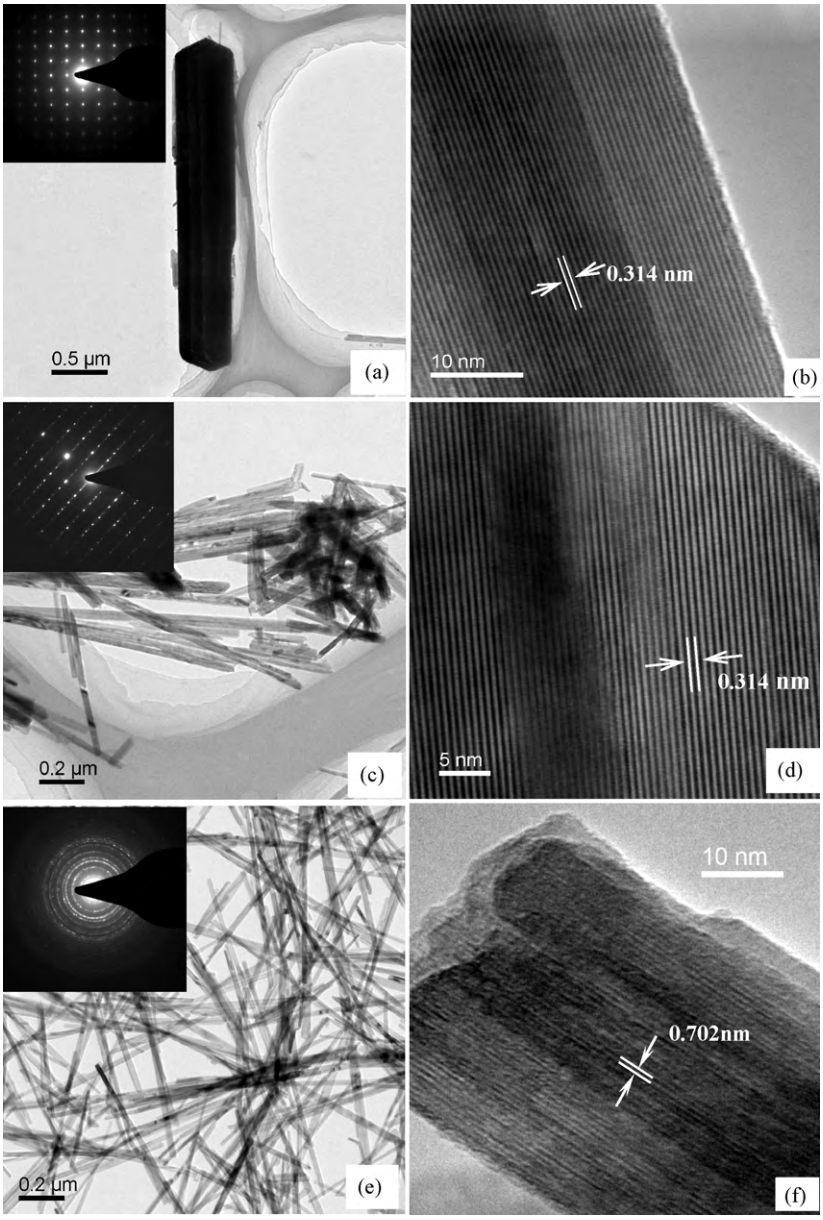

Fig. 3. The SAED patterns (a, c, e) and HRTEM (b, d, f) of the MnO_2 products synthesized with different $KMnO_4$ concentrations at 160 °C: (a and b) 0.025 M, (c and d) 0.0625 M, (e and f) 0.125 M.

tric phenomenon of MnO_2 materials. Studies on electromagnetic properties of ferrite materials doped with MnO_2 have supported this point of view [22–24]. The studies have shown that the introduction of MnO_2 into NiCuZn ferrite materials can decrease their magnetostriction constant and so as to increase the initial permeability and dissipation factor significantly, due to the space charge polarization of MnO_2 material [22,23]. The dielectric loss tangents, piezoelectric coefficients and Curie temperatures of $Pb(Zr, Ti)O_3$ (PZT) materials are also affected by MnO_2 substitution [24].

For MnO_2 materials, an assembly of space charge carriers requires finite time to line up with their axes parallel to the alternating electric field. With the reversal increase of field frequency, the space charge carriers will not keep up with the field and the alternation of their direction lags behind that of the external field, thus resulting in a reduction in the dielectric constant of materials, which is also the so-called dispersive phenomenon of MnO_2 composites [25].

For a dielectric material, the dielectric permittivity implies the polarization of the material under an electromagnetic field, which is depended mainly on the particle morphology and its interior crystalline structure besides external factors such as frequency, pressure and temperature. From Fig. 2, one can see that the as-prepared MnO_2 materials with different reactant concentrations have various crystalloid states and morphologies, and so have different dielectric properties.

As to the increasing dielectric permittivity with temperature, it can be due to the increasing thermal energy. Dielectric permittivity implies the polarization degrees of MnO_2 materials under the external electromagnetic field. The more dipoles exist in the field, the larger the permittivity is. With the increasing of temperature, more of the localized dipoles liberate and align their directions with the field, thus results in a larger polarizability as well as an increase in ε' [26].

Fig. 5 shows the relation between the dielectric loss tangents ($\varepsilon''/\varepsilon'$) and the absolute temperature (K) at frequencies of

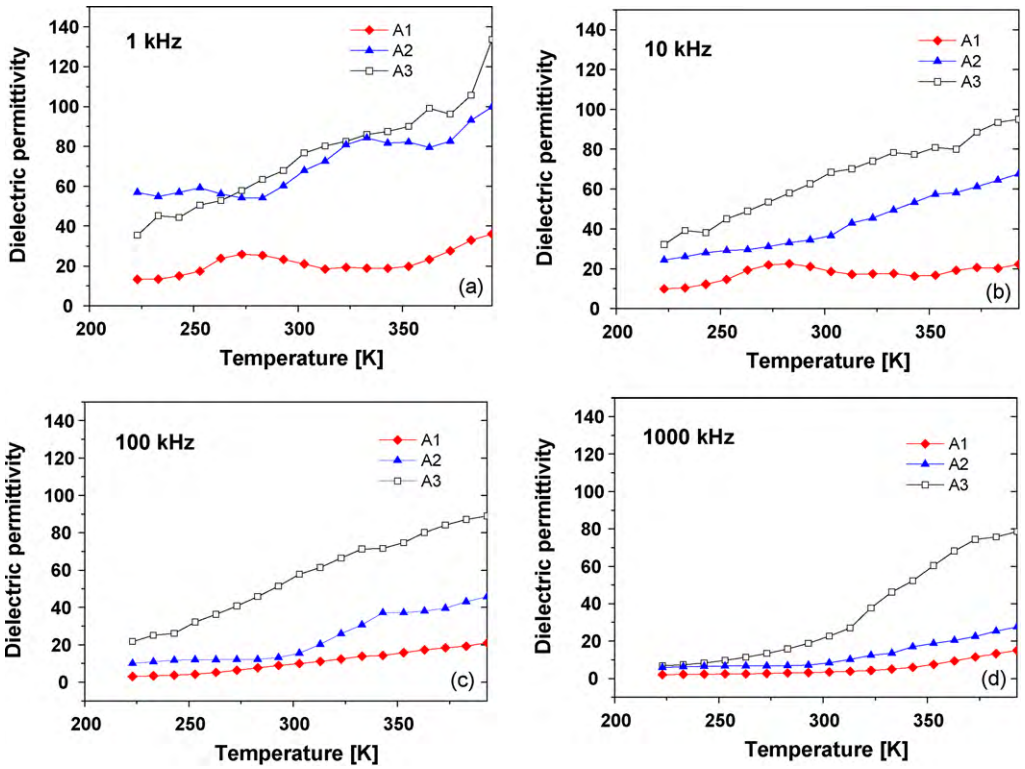

Fig. 4. Temperature dependent of real permittivity of samples A1, A2 and A3 at different frequencies: (a) 1 kHz, (b) 10 kHz, (c) 100 kHz, (d) 1000 kHz.

1 kHz, 10 kHz, 100 kHz and 1000 kHz for samples A1, A2 and A3 in the temperatures ranging from 223 K to 390 K. It reveals that the dielectric loss tangents increase with the temperature and decrease with the testing frequency, which is the same trend as dielectric permittivity shown in Fig. 4. With a closer look at Fig. 5, one can see that sample A2 has the greatest dielectric loss values within the three samples, and with the increasing of temperature and frequency, the dielectric loss dif-

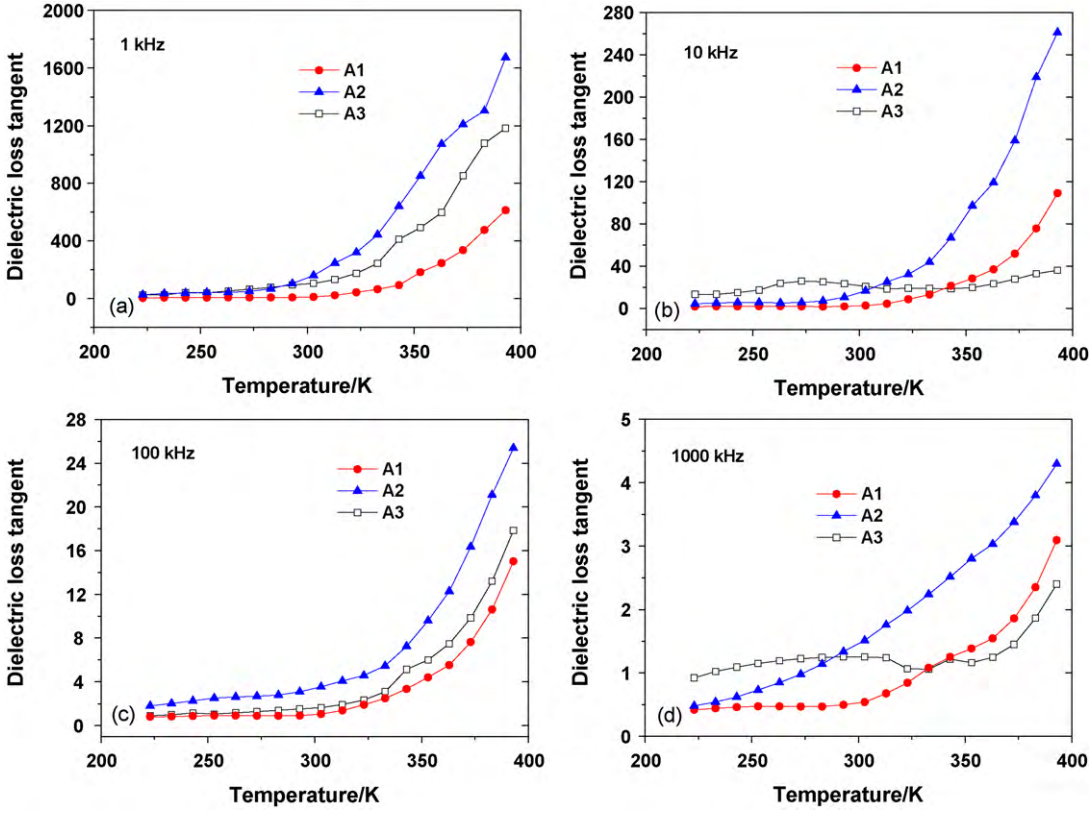

Fig. 5. Temperature dependent of dielectric loss tangents of samples A1, A2 and A3 at different frequencies: (a) 1 kHz, (b) 10 kHz, (c) 100 kHz, (d) 1000 kHz.

ferences between sample A2 and the other two samples turns to be larger.

The differences of dielectric loss tangents can be ascribed to the particle morphology and crystallinity variations of the three samples. As is known, dielectric loss tangent implies the polarization ability of a material under an external electromagnetic field. The variations of crystalloid states of the MnO_2 materials can result in the change of crystal lattice, the differences of crystal defects and holes, which all play key roles on the polarization of the materials [2]. The morphological structure variations also induce different extinction cross-sections, and so result in various electromagnetic polarization abilities. The stronger the polarization, the greater the dielectric loss is. For the as-prepared MnO_2 materials, particles with different reactant concentrations have different crystalline phases and morphological shapes, so they have various dielectric loss tangents.

It is proposed that there is an incident wave propagating along the x direction reaches a particle filling composite material at negligible multiple scattering. The electromagnetic energy in the material through a thickness of x is [27]:

$$I = I_0 \exp(-n\sigma_{ex}x) = I_0 \exp\left(\frac{(-f(\sigma_{ab}+\sigma_{sc})x}{\upsilon}\right) \quad (5)$$

in which I_0 and I are the energy intensity at the material surface and through a thickness x in the material, respectively. σ_{ex}, σ_{ab} and σ_{sc} are the extinction cross-section (ECS), absorption cross-section (ACS) and scattering cross-section (SCS) of the particle. f and υ refer to the bulk concentration and volume of each particle. n is the number of particles in a unit volume of composite material. For the material with MnO_2 particles dispersed randomly in the PVA matrix, σ_{ab} and σ_{sc} can be expressed as [28]:

$$\sigma_{sc} = \frac{k^4}{18\pi}\sum_{t=x,y,z}\left(\left|\chi_e^t\right|^2 + \left|\chi_m^t\right|^2\right) \quad (6)$$

$$\sigma_{ab} = \frac{1}{3}k\sum_{t=x,y,z} Im\left(\chi_e^t + \chi_m^t\right) \quad (7)$$

where χ_e^t and χ_m^t refer to the dielectric polarizability and magnetic susceptibility of the particulate inclusions [29]:

$$\chi_e^t = \frac{\upsilon(\varepsilon_1-\varepsilon)}{\varepsilon + N_t(\varepsilon_1-\varepsilon)}, \quad \chi_m^t = \frac{\upsilon(\mu_1-\mu)}{\mu + N_t(\mu_1-\mu)} \quad (8)$$

where ε and μ, ε_1 and μ_1 are the dielectric constants and magnetic permeability of MnO_2 particles and PVA matrix, respectively. N_t (t = x, y, z) is the depolarization factor of the particle in the x, y and z direction. For particles with different morphological shapes, N_t has different values.

For the ACS and SCS of particles with spherical, flake and acicular shapes, it is found that the particles with acicular or needle-like shapes have the most extinction cross-sections and better electromagnetic wave attenuation properties if the inclusion particle has larger permittivity and permeability than the matrix [28]. From Figs. 2 and 3, sample A1 mainly consists of massive β-MnO_2 microrods with much larger diameter and less aspect ratio, and sample A3 mainly includes α-MnO_2 needle-like nanorods with much less diameter and larger aspect ratio than A1. Therefore, it has much better dielectric loss than A1.

As for a particle filling composite material, morphology of the filling inclusions is only one of the many factors that influence the dielectric properties of the composite, and the dispersion homogeneousness of the filling inclusions is the second but not less important factors. The sample A3 has much larger aspect ratio, but nanowires and nanorods are prone to be tangled with each other to form aggregates due to their much larger surface energy, and thus deteriorates their polarization abilities and so does the dielectric loss tangents. As to sample A2, it has nanowires and microrods with larger diameters. Microrods have less polarization ability than nanowires, but the existence of microrods can greatly improve the dispersion of nanowires in the PVA matrix and thus decrease the amounts and size of nanowires aggregations [30], and so improve the polarization of sample A2. Moreover, the nanowires and microrods in sample A2 will be all polarized under an external electromagnetic field [2], which also results in the improvement of the dielectric loss tangents of sample A2.

4. Conclusions

MnO_2 materials with different crystal structures and morphologies were prepared by hydrothermal methods at 160 °C for 48 h with different reactant concentrations. The as-prepared MnO_2 gradually transformed from β-MnO_2 microrods to α-MnO_2 nanowires and nanorods with the different $KMnO_4$ concentrations from 0.025 M to 0.125 M. The studies of the dielectric properties show that the real parts of permittivity and dielectric loss tangents of the samples decrease with the increase of frequency tested. And the dielectric permittivity and dielectric loss tangents all increase with the increasing temperature from 223 K to 393 K. The α-MnO_2 nanorods prepared with the highest $KMnO_4$ concentration show the best permittivity values at the whole frequency band of 1–1000 kHz, and the products prepared with moderate $KMnO_4$ concentration, which contains both nanowires and microrods, have the best dielectric loss tangents at the whole temperature range tested. The dielectric loss of manganese dioxide can be mainly ascribed to space charge polarization and interface polarization.

Acknowledgements

This work was financially supported by the Natural Science Foundation of China (No. 20901066) and the Foundation of Yunnan Provincial Educational Committee (No. 08Y0042).

References

[1] X. Wang, Y.D. Li, Chem. Eur. J. 9 (2003) 300–306.
[2] Y.P. Duan, H. Ma, X.G. Li, S.H. Liu, Z.J. Ji, Physica B 405 (2010) 1828–1831.
[3] R.N. Rddy, R.G. Reddy, J. Power Sources 132 (2004) 315–320.
[4] Y. Chen, C. Liu, F. Li, H. Cheng, J. Alloys Compd. 397 (2005) 282–285.
[5] M.M. Thacheray, Prog. Solid State Chem. 25 (1997) 1–71.
[6] C.A. Frysz, X. Shui, D.D.L. Chung, J. Power Sources 58 (1996) 41–54.
[7] X. Zhang, Y. Duan, H. Guan, S. Liu, B. Wen, J. Magn. Magn. Mater. 311 (2007) 507–511.
[8] H. Sato, T. Enoki, M. Isobe, Y. Ueda, Phys. Rev. B 61 (2000) 3563–3569.
[9] Y. Duan, Y. Yang, H. Ma, S. Liu, J. Phys. D: Appl. Phys. 41 (2008) 125403.
[10] D. Yan, S. Cheng, R.F. Zhuo, J.T. Chen, J.J. Feng, H.T. Feng, H.J. Li, Z.G. Wu, J. Wang, P.X. Yan, Nanotechnology 20 (2009) 105706.
[11] H. Guan, S. Liu, Y. Zhao, Y. Duan, J. Electron. Mater. 35 (2006) 892–896.
[12] H. Guan, Y. Zhao, S. Liu, S. Lv, Eur. Phys. J. Appl. Phys. 36 (2006) 235–239.
[13] X.M. Liu, S.Y. Fu, C.J. Huang, Powder Technol. 154 (2005) 120–124.
[14] G.H. Yue, P.X. Yan, D. Yan, D.M. Qu, X.Y. Fan, M.X. Wang, H.T. Shang, J. Cryst. Growth 294 (2006) 385–388.
[15] G.L. Wang, B. Tang, L.H. Zhuo, J.C. Ge, M. Xue, Eur. J. Inorg. Chem. 2006 (2006) 2313–2317.
[16] X.L. Shi, M.S. Cao, X.Y. Fang, J. Yuan, Y.Q. Kang, W.L. Song, Appl. Phys. Lett. 93 (2008) 223112.
[17] Y.F. Shen, S.L. Suib, C.L. O'Young, J. Am. Chem. Soc. 116 (1994) 11020–11029.
[18] X. Zhang, W. Yang, J. Yang, D. Evans, J. Cryst. Growth 310 (2008) 716–722.
[19] W.C. Kao, Dielectric Phenomena in Solids, Elsevier Academic Press, CA, 2004.
[20] K.S. Cole, R.H. Cole, J. Chem. Phys. 9 (1941) 341–351.
[21] X. Xia, Battery Bimonthly 34 (2004) 411–414.
[22] J.H. Nam, W.G. Hur, J.H. Oh, J. Appl. Phys. 81 (1997) 4794–4796.
[23] Z.X. Yue, J. Zhou, L.T. Li, Z.L. Gui, J. Magn. Magn. Mater. 233 (2001) 224–229.
[24] Y.D. Hou, M.K. Zhu, F. Gao, H. Wang, B. Wang, H. Yan, C.S. Tian, J. Am. Ceram. Soc. 87 (2004) 847–850.

[25] B.P. Rao, K.H. Rao, J. Mater. Sci. 32 (1997) 6049–6054.
[26] M.A. Ahmad, E. Ateia, L.M. Salah, A.A. El-Gamal, Phys. Status Solidi (a) 201 (2004) 3010–3022.
[27] C.F. Bohren, D.R. Huffman, Absorption and Scattering of Light by Small Particles, A Wiley-International Publication, 1983.
[28] F.D. Ge, J. Zhu, L.M. Chen, Acta Electron. Sin. 24 (1996) 82–86.
[29] A. Priou, Dielectric Properties of Heterogeneous Mixtures, Elsevier Publication, New York, 1991.
[30] P.W. Chen, D.D.L. Chung, J. Electron. Mater. 24 (1995) 47–51.